The Astrophysical Journal, 924:62 (11pp), 2022 January 10 https://doi.org/10.3847/1538-4357/ac33a4

The Space Density of Ultra-luminous QSOs at the End of Reionization Epoch by the QUBRICS Survey and the AGN Contribution to the Hydrogen Ionizing Background

Andrea Grazian[1], Emanuele Giallongo[2], Konstantina Boutsia[3], Giorgio Calderone[4], Stefano Cristiani[4,5,6], Guido Cupani[4,6], Fabio Fontanot[4,6], Francesco Guarneri[4,7], and Yacob Ozdalkiran[8]
[1] INAF–Osservatorio Astronomico di Padova, Vicolo dell'Osservatorio 5, I-35122, Padova, Italy; andrea.grazian@inaf.it
[2] INAF–Osservatorio Astronomico di Roma, Via Frascati 33, I-00078, Monte Porzio Catone, Italy
[3] Las Campanas Observatory, Carnegie Observatories, Colina El Pino, Casilla 601, La Serena, Chile
[4] INAF–Osservatorio Astronomico di Trieste, Via G.B. Tiepolo, 11, I-34143, Trieste, Italy
[5] INFN-National Institute for Nuclear Physics, via Valerio 2, I-34127 Trieste
[6] IFPU–Institute for Fundamental Physics of the Universe, via Beirut 2, I-34151, Trieste, Italy
[7] Dipartimento di Fisica, Sezione di Astronomia, Università di Trieste, via G.B. Tiepolo 11, I-34131, Trieste, Italy
[8] Ecole Polytechnique Paris, Rte de Saclay, F-91120, Palaiseau, France
Received 2021 July 21; revised 2021 October 8; accepted 2021 October 25; published 2022 January 12

Abstract

Motivated by evidences favoring a rapid and late hydrogen reionization process completing at $z\sim5.2$–5.5 and mainly driven by rare and luminous sources, we have reassessed the estimate of the space density of ultra-luminous QSOs at $z\sim5$ in the framework of the QUBRICS survey. A $\sim90\%$ complete sample of 14 spectroscopically confirmed QSOs at $M_{1450}\leqslant-28.3$ and $4.5\leqslant z\leqslant5.0$ has been derived in an area of 12,400 deg^2, thanks to multiwavelength selection and Gaia astrometry. The space density of $z\sim5$ QSOs within $-29.3\leqslant M_{1450}\leqslant-28.3$ is three times higher than previous determinations. Our results suggest a steep bright-end slope for the QSO luminosity function at $z\sim5$ and a mild redshift evolution of the space density of ultrabright QSOs ($M_{1450}\sim-28.5$) at $3<z<5.5$, in agreement with the redshift evolution of the much fainter active galactic nucleus (AGN) population at $M_{1450}\sim-23$. These findings are consistent with a pure density evolution for the AGN population at $z>3$. Adopting our $z\sim4$ QSO luminosity function and applying a mild density evolution in redshift, a photoionization rate of $\Gamma_{\rm HI}=0.46^{+0.17}_{-0.09}\times10^{-12}$ s^{-1} has been obtained at $z=4.75$, assuming an escape fraction of $\sim70\%$ and a steep faint-end slope of the AGN luminosity function. The derived photoionization rate is ~50–100% of the ionizing background measured at the end of the reionization epoch, suggesting that AGNs could play an important role in the cosmological reionization process.

Unified Astronomy Thesaurus concepts: Reionization (1383); Active galactic nuclei (16); Surveys (1671)

1. Introduction

At $z<10$, the Universe underwent a "disruptive" phase transition, usually called reionization, causing the neutral hydrogen fraction to drop from unity to a value of $\sim10^{-4}$ at $z<5$–6, after which the Universe was almost completely ionized (Fan et al. 2006). The low optical depth of the cosmic microwave background (CMB) photons measured by the Planck satellite (Planck Collaboration et al. 2020) supports such a scenario with a midpoint redshift $z\lesssim7$. However, the timing and topology of reionization is still unclear, especially because we do not know the relative contribution of star-forming galaxies and AGNs to the hydrogen (HI) ionizing background in the Universe close to the reionization epoch. Moreover, while in the past few years this process was thought to start early and developing in a relatively large redshift interval $6<z<15$ (e.g., Bouwens et al. 2009), there are now accumulating undisputed evidences in favor of a late and short reionization process.

The strong redshift evolution of the mean free path (mfp) of ionizing photons into the intergalactic medium (IGM), which appears to decrease significantly in the redshift interval $4<z<6$, could be indicative of a rapid change in the ionization level of the IGM since, for a given source emissivity, the photoionization rate $\Gamma_{\rm HI}$ is simply proportional to the mfp. Indeed a fast drop of the mfp at $z\sim6$ has been recently derived by Becker et al. (2021) with respect to the extrapolation from values measured at lower redshifts (Worseck et al. 2014).

Additional support to a quick and late reionization scenario is provided by several independent observations, including (1) the rapid drop of the space density of Lyα emitters (LAEs) at $z>6$ (Morales et al. 2021), (2) the rapid decrease of the fraction of LAEs within the Lyman-break galaxy population at $z\sim6$–7 (Hoag et al. 2019), and (3) the detection of the patchy kinetic Sunyaev–Zeldovich (kSZ) effect, indicating a short duration phase $\Delta z\leqslant1$–2.8 of the reionization event (George et al. 2015; Reichardt et al. 2021). All these observational evidences suggest that the $z\gtrsim7$ IGM should be almost neutral, with $x_{\rm HI}>0.6$. This implies a rapid reionization process that is effective in the short redshift interval $5\lesssim z\lesssim6.5$. In this rapid and late reionization scenario, sparse overdensities of neutral hydrogen are still present at redshifts as low as $z\sim5.2$ in the diffuse ionized IGM, implying an end of reionization at $z\sim5$ (Keating et al. 2020; Bosman et al. 2021; Zhu et al. 2021).

A rapid and late reionization scenario is in tension with models assuming galaxies as the only contributors to the budget of HI ionizing background. Indeed, models assuming star-forming galaxies as main contributors to the UV background show that (relatively faint) galaxies tend to start the reionization process too early (Naidu et al. 2020). It is also

worth noting that UV selected star-forming galaxies do not show an abrupt drop in their UV luminosity density at $z\sim5.5$, where the bulk of the reionization event is taking place, but they show an accelerated evolution only at $z\sim8-9$ (Oesch et al. 2018; Bouwens et al. 2021), too early to be in agreement with the redshift evolution shown by the mfp measured by Becker et al. (2021) and by the photoionization rate (Calverley et al. 2011; Wyithe & Bolton 2011; Davies et al. 2018).

Moreover, an escape fraction of ionizing photons from galaxy halos of $f_{\rm esc}\sim10\%$ for the global galaxy population down to $M_{1500}\sim-12$ (Kuhlen & Faucher-Giguère 2012; Robertson et al. 2015; Finkelstein et al. 2019) would be needed to accomplish the rapid evolution of the mfp. Such a value for $f_{\rm esc}$ is much higher than what is directly measured in galaxies at lower redshifts ($z=3$–4; e.g., Grazian et al. 2016, 2017; Pahl et al. 2021). This tension would require rapid evolution in the physical properties of the global galaxy population (Davies et al. 2021) or relaxing somewhat the constraints derived from the mfp measurements (Cain et al. 2021). The difficulty in ascribing the photon budget, needed to drive this quick and late reionization, to the global galaxy population alone, leaves room to a significant role of the AGN population in providing a significant photoionization rate at late cosmic times ($z<6.5$) and an acceleration to the reionization process.

AGNs indeed are known to ionize their environment, producing a remarkable proximity effect in their Lyα forest absorption spectra. This enhancement in the ionization level of the IGM due to the ionizing QSO flux extends to several proper megaparsecs (∼6–10 pMpc) as observed in bright QSOs ($M_{1450}\lesssim-27$; Fan et al. 2006; Calverley et al. 2011; Eilers et al. 2017). This implies that their escape fraction is in general relatively large (∼70%) and appears to keep values >50% in fainter AGNs ($M_{1450}\lesssim-23$; Cristiani et al. 2016; Grazian et al. 2018; Romano et al. 2019). Thus, the relevance of AGNs in the reionization process mainly depends on the space density evolution of AGNs with $M_{1450}<-22$ in the redshift interval $3.5<z<6.5$. However, the assessment of their space density at very high redshifts is challenging both for relatively bright QSOs and fainter AGNs, requiring a wide multiwavelength approach and ancillary selection techniques derived e.g., by the astrometric and/or variability analyses.

At $z\sim4$–4.5 there is an agreement among different spectroscopic and photometric surveys based on multiwavelength data, suggesting a double power-law shape for the luminosity function with a break at $M_{1450}\sim-26\div-26.5$ (Glikman et al. 2011; Boutsia et al. 2018; Giallongo et al. 2019; Boutsia et al. 2021) and a steep bright-end slope $\beta\sim-3.7\div-4$. This luminosity function is higher with respect to previous standard color-selected surveys (Akiyama et al. 2018; Schindler et al. 2019a, 2019b), both at bright and intermediate magnitudes near the break.

While at redshift $z\gtrsim6$, we have only scanty data mainly confined to bright QSOs, an increasing data set coming from spectroscopic and photometric surveys is progressively available at $z\sim5$, based on more sophisticated selection criteria. In this context, we present here an estimate of the space density of luminous QSOs selected in a homogeneous way within the Quasars as Bright Beacons for Cosmology in the Southern Hemisphere (QUBRICS) Survey (Calderone et al. 2019; Boutsia et al. 2020). This survey turned out to be particularly efficient (∼70%) and complete (∼80%) in finding very bright QSOs at high z (Boutsia et al. 2021). This project, joining together state-of-the-art surveys like Skymapper, Gaia, and WISE, is opening a new era of QSO searches at high z. Adopting the best-fit QSO luminosity function derived at $z\sim4$ in our previous work and applying the redshift evolution in the space density derived from the present work, we improve the estimate of the AGN photoionization rate at $z\sim5$.

The structure of this paper is the following: in Section 2, we describe the QUBRICS survey, the selection of $z\sim5$ QSOs and their completeness. In Section 3, we derive the QSO luminosity function at $M_{1450}\sim-28.5$, discussing the evolution of the QSO space density with redshift, and we compute the photoionization rate produced by QSOs at $z\sim5$. We discuss the reliability of these results in Section 4, providing the concluding remarks and summary in Section 5. Throughout the paper, we adopt the Λ cold dark matter (Λ-CDM) concordance cosmological model ($H_0=70$ km s^{-1} Mpc^{-1}, $\Omega_M=0.3$, and $\Omega_\Lambda=0.7$). All magnitudes are in the AB photometric system.

2. Data

2.1. The QUBRICS Survey

The QUBRICS Survey aims at finding the brightest high-z QSOs in the Southern hemisphere (Calderone et al. 2019; Boutsia et al. 2020; hereafter PaperI and PaperII, respectively) by adopting the canonical correlation analysis (CCA) machine-learning techniques applied to wide multiwavelength databases (e.g., Skymapper, Gaia, WISE). The first pilot exploratory observations revealed relatively high efficiencies, of ∼80%. After many observations, the QUBRICS Survey produced a list of more than 250 new bright ($i_{\rm psf}\leqslant18.0$) QSOs at $z>2.5$, assessing the success rate to ∼70% and the completeness to ∼80%. The success rate of finding QSOs at $z>4.5$ for the QUBRICS survey is 1.6%, much lower than at $z>2.5$, since the original goal of our survey was to find objects at $z\sim3$. Meanwhile, other high-z bright QSOs are going to be discovered by QUBRICS, thanks to the exploitation of new state-of-the-art machine-learning techniques, e.g., probabilistic random forest (PRF; Guarneri et al. 2021) or extreme gradient boosting (XGB; Calderone et al. in prep.).

The new high-z QSOs discovered by the QUBRICS Survey are going to be used to feed efficient high-resolution spectrographs in order to study the properties of the IGM or to carry out tests of fundamental physics (see e.g., PaperII for a discussion of the Sandage Test). Since the QUBRICS project turns out to be an efficient survey, but also a complete one, it has been used in Boutsia et al. (2021) to derive the luminosity function of $z\sim4$ QSOs at unprecedented high luminosities ($M_{1450}\leqslant-28.0$). In this paper we extend this analysis at $4.5<z<5.0$, where information on the ultrabright active SMBH population is still scanty.

2.2. Selection of Ultrabright QSOs at z ∼ 5 in the QUBRICS Survey

The main sample of QUBRICS described in PaperII has been adopted in order to select spectroscopically confirmed QSOs at $4.5\leqslant z_{\rm spec}\leqslant5.0$ with an i-band magnitude brighter than $i_{\rm psf}=18.0$. Table 1 includes 14 QSOs that satisfy the above criteria. The spectroscopic confirmation of these high-z QSOs have been carried out by the QUBRICS team (PaperI, PaperII), as well as by other independent observations (e.g., Véron-Cetty & Véron 2010; Schindler et al. 2019a, 2019b; Wolf et al. 2020). It is worth noting that all these different

Table 1
The $i_{psf} \leqslant 18.0$ QSO sample at $4.5 \leqslant z_{spec} \leqslant 5.0$ in the QUBRICS Survey

$ID_{Skymapper}$ DR1.1	R.A. J2000	Decl. J2000	z_{spec}	i_{psf} AB	i_{psf}^{err}	M_{1450}	z_{cca}	z_{spec} References
7596895	00:05:00.19	−18:57:15.43	4.560	17.82	0.03	−28.450	3.64	Wolf20
317802750	00:12:24.99	−48:48:29.86	4.621	17.72	0.17	−28.588	5.44	PaperII, Wolf20
7869715	01:35:39.28	−21:26:28.42	4.940	17.99	0.08	−28.460	4.77	Wolf20
318204033	03:07:22.89	−49:45:48.24	4.728	17.41	0.04	−28.974	4.87	P01, Veron10
10431842	03:55:04.85	−38:11:42.41	4.545	17.82	0.16	−28.467	4.42	P01, Veron10
54680559	11:10:54.68	−30:11:29.88	4.779	17.35	0.03	−29.035	4.59	PaperII, PSELQS, Wolf20
65100743	12:05:23.13	−07:42:32.65	4.690	17.88	0.03	−28.455	5.18	R06, Veron10
3436512	21:11:05.60	−01:56:04.14	4.891	17.91	0.02	−28.526	5.56	PaperI, Wolf20
304245360	21:19:20.85	−77:22:53.17	4.558	17.86	0.07	−28.412	4.93	PaperI, Wolf20
397340	21:57:28.21	−36:02:15.11	4.771	17.37	0.02	−29.009	5.05	PaperII, Wolf20
4368005	22:21:52.88	−18:26:02.87	4.520	17.87	0.08	−28.379	3.11	PSELQS
5392050	22:39:53.67	−05:52:19.81	4.558	17.95	0.09	−28.321	1.58	SL96, Veron10
1913850	23:04:29.88	−31:34:27.02	4.840	17.77	0.04	−28.636	4.69	Wolf20
308375290	23:35:05.86	−59:01:03.33	4.540	17.60	0.02	−28.664	5.36	PaperII, Wolf20

Note. The references for z_{spec} are: SL96 refers to Storrie-Lombardi et al. (1996); P01 refers to Péroux et al. (2001); R06 refers to Riechers et al. (2006); Veron10 refers to Véron-Cetty & Véron (2010); PSELQS refers to Schindler et al. (2019b); Wolf20 refers to Wolf et al. (2020).

groups carried out independent surveys; nonetheless, several high-z QSOs in the southern hemisphere have been recently confirmed in multiple surveys, as indicated in the last column of Table 1.

The absolute magnitudes at 1450 Å rest-frame wavelengths (M_{1450}) in Table 1 have been derived following Boutsia et al. (2021). Starting from the apparent i_{psf} magnitudes of Skymapper and from the spectroscopic redshifts, the equation

$$M_{1450} = i_{psf} - 5\log(d_L) + 5 + 2.5\log(1 + z_{spec}) + K_{corr} \quad (1)$$

has been adopted, where d_L is the luminosity distance expressed in parsec (pc). The k-correction K_{corr} is given by the expression

$$K_{corr} = -2.5\alpha_\nu \log_{10}(\lambda_{obs}/(1 + z_{spec})/\lambda_{rest}), \quad (2)$$

where the adopted spectral slope of QSOs is $\alpha_\nu = -0.7$, $\lambda_{rest} = 1450$ Å, and $\lambda_{obs} = 7799$ Å is the central wavelength of the i_{psf} filter.

Alternatively, the absolute magnitudes M_{1450} can be derived from the calibrated spectra, as carried out by e.g., Glikman et al. (2010). In order to check the consistency of the M_{1450} from imaging with that from spectroscopy, we carry out the calculation of the k-corrections for the six QSOs in Table 1 observed by QUBRICS. The difference between the two k-corrections is -0.087 ± 0.020. This confirms that the absolute magnitudes derived from the i_{psf} apparent magnitudes are consistent with the one derived from the spectra at the $\lesssim$10% level. In the following, we will adopt the absolute magnitudes M_{1450} derived from photometry.

2.3. Completeness of z ∼ 5 QSO Sample

In order to estimate the completeness of the QSO sample in Table 1, it is useful to consider the results obtained by similar surveys. Wolf et al. (2020) searched for bright QSOs at $z > 4.5$ using data from SkyMapper, Gaia, and WISE. They found 23 QSOs at $4.5 \leqslant z_{spec} \leqslant 5.0$ and $M_{1450} \leqslant -28.0$ in 12,500 deg^2 in the southern hemisphere. Since their survey area is similar to the QUBRICS one (12,400 deg^2), and their magnitude cut is similar to the one adopted here, it is surprising that they retrieve 65% more QSOs than in our sample. Checking Table 1 carefully, however, it is evident that our sample is limited to slightly brighter magnitudes ($M_{1450} \leqslant -28.3$) than their limit. If the Wolf et al. (2020) sample is restricted to $M_{1450} \leqslant -28.3$, 19 QSOs are left, reducing the discrepancy with our sample within the mutual statistical uncertainties.

Of the 23 QSOs by Wolf et al. (2020) with $4.5 < z < 5.0$ and $M_{1450} \leqslant -28.0$, only 12 objects are part of our QUBRICS sample. Nine QSOs of Wolf et al. (2020) have an i-band magnitude in Skymapper DR1.1 fainter than 18.0, so out of the QUBRICS selection criteria. Two QSOs of Wolf et al. (2020) have $i_{psf} < 18.0$, but they are not part of our sample. For one of these two QSOs (J151443.82–325024.8), the galactic latitude is below the adopted threshold in PaperI and PaperII, i.e., $|g_{lat}| \geqslant 25^{deg}$, and thus it does not belong to our main sample. Only one QSO, J145147.04–151220.1 at $z_{spec} = 4.76$, has a $i_{psf} = 17.1826$ in Skymapper DR2, but it is not extracted by Skymapper DR1.1. It is worth noting that this is a very bright QSO ($M_{1450} = -29.29$ in Wolf et al. 2020), and it is missing from our sample, since the QUBRICS survey has been based on Skymapper DR1.1. Based on this comparison, a simple determination of the completeness of the QUBRICS sample can be estimated of the order of 92.3% (12/13). Two objects in our sample are not present in Wolf et al. (2020), indicating that the completeness level of their survey is ∼90%. It is worth noting that the completeness correction for bright QSOs at $z \sim 4$ in the QUBRICS survey is slightly lower, of ∼84%, as discussed in Boutsia et al. (2021). Recently, Onken et al. (2021) have released an incremental sample of 119 new QSOs at $z > 4$. We have checked that they are all fainter than our magnitude limit of $i_{psf} = 18.0$, so it is not possible to use their results for a refinement of the completeness calculation for the QUBRICS survey.

It is possible to estimate the incompleteness in an alternative way, as discussed in Boutsia et al. (2021). The main sample of QUBRICS has been extracted from the Skymapper DR1.1 database, but it is possible that this survey is not complete. We have used the Dark Energy Survey (DES; Abbott et al. 2021) to select all the known QSOs at $4.5 < z < 5.0$ and $M_{1450} \leqslant -28.0$. We have found five QSOs in a ∼5000 deg^2 area satisfying these criteria. Of these five QSOs, only four objects have an

Table 2
The $1/V_{\rm max}$ space density Φ of $4.5 \leqslant z \leqslant 5.0$ QSOs in the QUBRICS footprint

Interval	$< M_{1450} >$	$N_{\rm QSO}$	Φ cMpc^{-3}	$\sigma_{\Phi}(up)$ cMpc^{-3}	$\sigma_{\Phi}(low)$ cMpc^{-3}
$-29.30 \leqslant M_{1450} \leqslant -28.30$	-28.60	14	3.115×10^{-10}	1.077×10^{-10}	8.251×10^{-11}

Note. The space density Φ has been corrected for incompleteness, as discussed in the main text. A completeness correction factor of 92.3% has been adopted in this case.

i-band magnitude determination in Skymapper DR1.1, indicating that the completeness of the latter is 80% (4/5). Given the low number statistics of the QSO sample based on DES, of only five objects, however, we prefer not to use this completeness in the following analysis.

Following Boutsia et al. (2021), another source of incompleteness is the fraction of candidates still awaiting for spectroscopic confirmations. Starting from the QUBRICS main sample in PaperII, there are seven objects with a photometric redshift (based on CCA) in the range $4.5 < z < 5.0$. Out of these seven candidates, five objects have been confirmed to be QSOs at $4.5 \leqslant z_{\rm spec} \leqslant 5.0$, and they are included in Table 1. Two candidates do not have yet spectroscopic identification, and future observations could increase the number of bright QSOs at $z \sim 4.8$. One of these two candidates, however, is slightly extended on the *i*-band of Skymapper, and for this reason it could be a bona-fide low-redshift object. In addition, there are three new QSO candidates at $z > 4.5$ selected with XGB and photometric redshifts, as will be described in future papers by this collaboration. We decide to not include in our completeness correction the term owing to the spectroscopic missing sample, but we are aware that the number of ultrabright QSOs at $z \sim 5$ could significantly increase in the future.

Based on the above considerations, we have decided to adopt as completeness factor for our sample the conservative 92.3% level derived above. We should take into account, however, that this estimate could be slightly lower (completeness of the order of ∼70–80%), as derived by the DES survey or taking into account the number of candidates still awaiting for spectroscopic identifications. In this case, the QSO space density at $z \sim 5$ would be even higher than the present estimates. Future spectroscopic follow-up observations would reduce the uncertainties on the completeness correction factor.

3. Determination of the Space Density of Ultrabright QSOs at $z \sim 5$.

We have derived the comoving space density of $4.5 < z < 5.0$ QSOs at $M_{1450} \lesssim -28$ by adopting the standard $1/V_{\rm max}$ approach, as described in detail in Boutsia et al. (2021). Due to the low number of bright QSOs in the QUBRICS survey, we decided to compute the space density in an absolute magnitude interval of $-29.3 \leqslant M_{1450} \leqslant -28.3$, that includes all the 14 QSOs in Table 1. The adopted lower bound in luminosity ($M_{1450} = -28.3$) corresponds to the magnitude limit of the survey in the *i*-band $i_{\rm psf} \leqslant 18.0$ at $z \sim 4.5$.

We have corrected the observed space density for incompleteness by adopting the correction factor of 92.3%, as discussed above. The derived space density Φ is associated to an absolute magnitude of $M_{1450} = -28.6$, the mean value of the QSOs in the ultrabright bin. Errors on Φ have been derived by adopting the Poissonian statistics, since $N_{QSO} > 10$. Table 2 summarizes the resulting space density Φ obtained from the QUBRICS survey.

The blue filled square in Figure 1 shows the space density Φ of $4.5 \leqslant z \leqslant 5.0$ QSOs in the QUBRICS footprint. For comparison, we have plotted in the same figure the determination of the QSO luminosity function by recent works at $z \sim 4$–5. When the mean redshift of these surveys is different from $z = 4.75$, their data points and curves have been shifted by adopting the pure density evolution recipe with $\gamma = -0.25$, as we will discuss in detail in Section 3.2. The green, red, dark green, and orange curves in Figure 1 show the best-fit luminosity functions of Kulkarni et al. (2019), Giallongo et al. (2019), Grazian et al. (2020), and Kim & Im (2021), respectively. The blue continuous line in Figure 1 is not the best fit to the QUBRICS data point, but it is the luminosity function of Boutsia et al. (2021) derived at $z \sim 3.9$ and evolved at $z = 4.75$ by adopting a pure density evolution recipe with $\gamma = -0.25$. The blue dashed line in Figure 1 is the same luminosity function as above, but with an *ad hoc* normalization, chosen to fit the QUBRICS data point at $z \sim 5$.

At these very bright luminosities ($M_{1450} \leqslant -28.5$), our space density is a factor of ∼3 higher than previous determinations by Yang et al. (2016), McGreer et al. (2018), and Niida et al. (2020), and higher than the best fit by Kulkarni et al. (2019), Giallongo et al. (2019), Grazian et al. (2020), and Kim & Im (2021). Since our luminosity function has been derived simply by dividing the number of confirmed QSOs at $z \sim 5$ by the cosmological volume of the Universe corresponding to $4.5 < z < 5.0$ and 12,400 sq. deg. area, with a small correction for completeness of 92.3%, it is quite surprising that Φ is significantly higher than literature estimations at the same redshifts. A possible explanation could be that the latter are heavily affected by strong incompleteness of a factor of ∼3. This is not surprising, however, given that it has been shown recently that even at $z \sim 4$ the previous determination of the QSO luminosity functions were incomplete by at least ∼30−40% (Schindler et al. 2019a, 2019b; Boutsia et al. 2021). A similar result at $M_{1450} \sim -28.5$ has been obtained by Onken et al. (2021) on a partially overlapping sky area. They find that the space density of $z \sim 5$ ultrabright QSOs is three times higher than previous determination by the Sloan Digital Sky Survey (SDSS), and it is similar to the one derived by the QUBRICS survey. This is a clear indication that the luminosity function from our sample is in agreement with these recent estimates, indicating that previous determinations in the past were possibly affected by severe incompleteness.

Summarizing, a first result, drawn from Figure 1, is that the space density of ultrabright QSOs at $z \sim 5$ is significantly higher, at least by a factor of 3, from previous determinations in the past, while it is fully consistent with the recent results by Wolf et al. (2020), Onken et al. (2021).

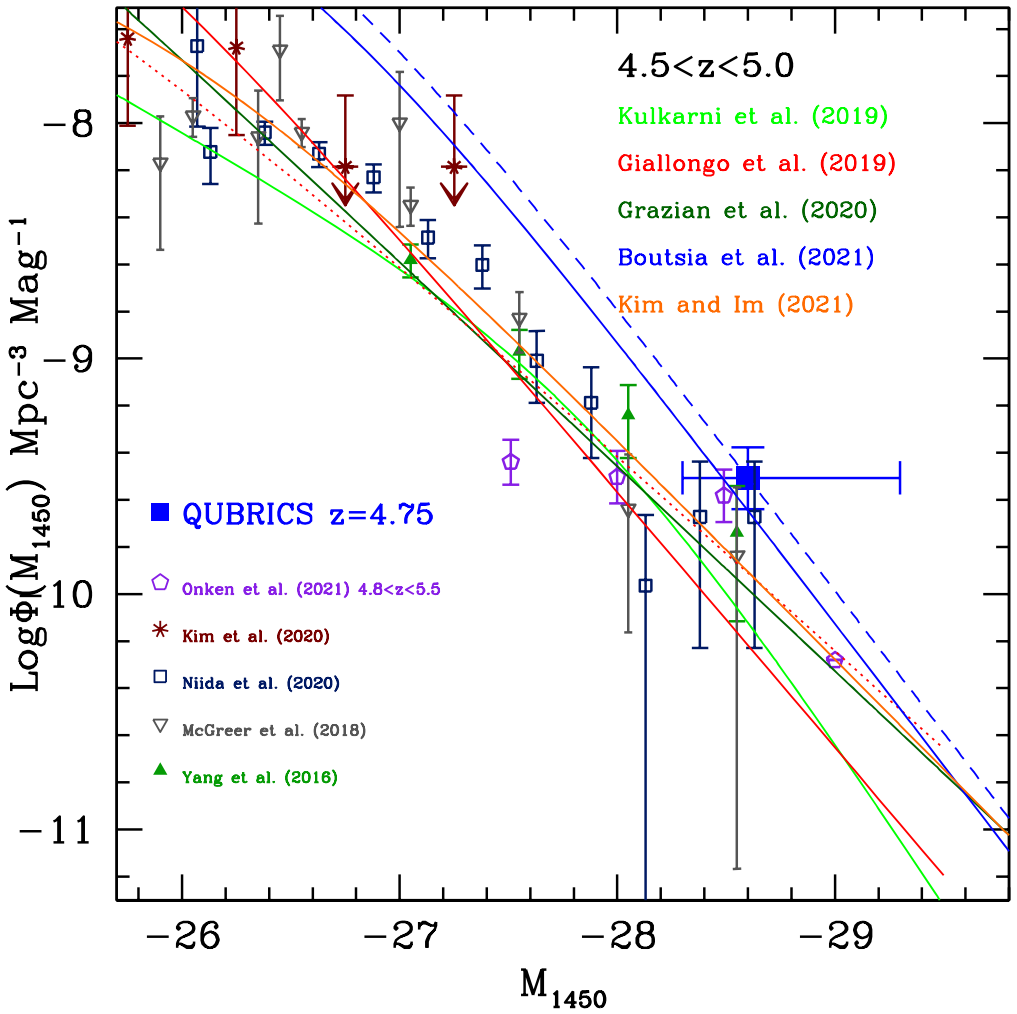

Figure 1. The luminosity function of QSOs at $4.5 \leqslant z_{\rm spec} \leqslant 5.0$ from QUBRICS (blue filled squares) compared to other luminosity functions from the recent literature. All the data points and curves have been shifted to $z = 4.75$, adopting a pure density evolution with $\gamma = -0.25$, as found in this work. The blue square indicates the mean absolute magnitude $\langle M_{1450} \rangle$ of the QSOs inside the bin, marked by the blue horizontal bar. The blue continuous line is not the fit to the data points, but it is the best fit of the QSO luminosity function at $z \sim 4$ by Boutsia et al. (2021), evolved at $z = 4.75$ with $\gamma = -0.25$, as well. The blue dashed line is the luminosity function of Boutsia et al. (2021), with a normalization factor that allows it to overlap with the observed nonparametric point from QUBRICS. The red dotted line is the model 3 of Giallongo et al. (2019), while the red continuous line is their model 4.

3.1. The Slope of the Bright End of the QSO Luminosity Function at z ∼ 5

The nonparametric space density derived in Figure 1 has limited information on the shape of the QSO luminosity function at $z \sim 5$. Despite the low number of QSOs in the QUBRICS survey and the relatively small range in luminosity covered by our sample, we try to constrain the bright-end slope by adopting the maximum-likelihood formalism by Marshall et al. (1983). Following Boutsia et al. (2021), we adopt a double power-law parameterization for the luminosity function:

$$\phi = \frac{\phi^*}{10^{0.4(M-M^*_{1450})(\alpha+1)} + 10^{0.4(M-M^*_{1450})(\beta+1)}}, \qquad (3)$$

where α and β are the faint and bright-end slopes of the luminosity function, M^*_{1450} is the absolute magnitude of the break, and ϕ^* is its normalization (which is not a free parameter of the Maximum Likelihood calculations). Fixing the knee of the luminosity function and the faint-end slope to $M^*_{1450} = -26.50$ and $\alpha = -1.85$, from the $z \sim 3.9$ parameterization provided by Boutsia et al. (2021), we obtain a best fit to the bright-end slope of $\beta = -4.64$, with a range between -6.19 and -3.43 at 68% confidence level probability. These values do not change if we fix the break to -26.0, since the QUBRICS data are limited to $M_{1450} \leqslant -28.30$, and consequently, they cannot provide any leverage on the break of the QSO luminosity function. If we leave as free parameters both the bright-end slope and the break, we obtain a 68% confidence interval of $\beta \leqslant -3.03$ and $M^*_{1450} \geqslant -29.80$. This indicates again that the break M^*_{1450} is practically unconstrained and the bright-end slope is relatively steep. If we divide our sample in two absolute magnitude intervals $-29.30 < M_{1450} < -28.80$ and $-28.80 < M_{1450} < -28.30$ and compute the nonparametric $1/V_{\rm max}$, then the resulting bright-end slope derived from these two points is $\beta = -4.48$, consistent with the previous values. The bright-end slope is still steep ($\beta = -4.97$) if we divide our sample in two uneven bins, containing seven objects each, i.e., $-29.30 < M_{1450} < -28.50$ and $-28.50 < M_{1450} < -28.30$. This is a starting indication that the bright-end slope of $z \sim 5$ QSO luminosity function is compatible with $\beta \sim -4$, as derived at lower redshifts by Schindler et al. (2019a, 2019b)

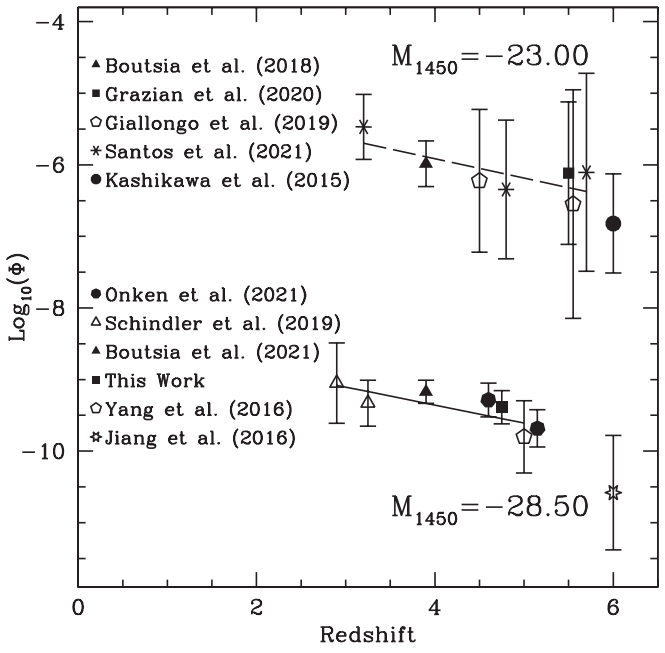

Figure 2. The space density of bright QSOs at $M_{1450} = -28.5$ and faint AGNs at $M_{1450} = -23.0$ at $z > 2.5$ from this work and recent surveys.

and Boutsia et al. (2021), and with $\beta = -3.84$ derived at $z \sim 5$ by Onken et al. (2021). We do not find an indication of a flattening of the bright-end slope of the QSO luminosity function going at high redshifts, as previously suggested by Fan et al. (2001, 2006), Jiang et al. (2008), Willott et al. (2010), and Masters et al. (2012).

3.2. The Evolution of the QSO Space Density with Redshift

Extrapolations of the blue lines in Figure 1 at absolute magnitudes fainter than $M_{1450} \sim -28$ are a factor of $\sim$3–5 above the previous determination of the QSO space densities at $z \sim 5$ by e.g., McGreer et al. (2018), Yang et al. (2016), Niida et al. (2020), Kim et al. (2020). Since the QUBRICS survey is typically sensible only to ultrabright QSOs at these redshifts, it is worth asking whether this dramatic disagreement is due to a strong incompleteness of the previous surveys at $M_{1450} \sim -26$ or, alternatively, if the extrapolations of the blue lines in Figure 1 to the faint end are too optimistic and the luminosity function of quasars near the break is indeed far lower. In order to provide a plausible answer to this question, we compare here the space densities of bright QSOs and faint AGNs at $z > 2.5$.

Figure 2 (bottom part) shows the space density of bright QSOs at $M_{1450} = -28.50$ as a function of the mean redshifts of the surveys at $z > 2.5$ collected from the literature. Fitting only the $z <= 5.0$ data, obtained by Schindler et al. (2019b) at $z = 2.90$ and 3.25, by the QUBRICS survey at $z = 3.9$ by Boutsia et al. (2021), at $z = 4.75$ (this work), and at $z = 5.0$ by Yang et al. (2016), we obtain a best-fit parameter of $\gamma = -0.25$, by adopting an evolution of the space density as $\Phi(z) = \Phi(z = 4.0) \cdot 10^{\gamma \cdot (z-4.0)}$. The continuous line in Figure 2 indicates the resulting best fit to the $z \leqslant 5.0$ data points at $M_{1450} = -28.50$. More interestingly, neglecting the $z = 5.0$ point by Yang et al. (2016), the evolution is even milder with $\gamma = -0.11$. The data point at $M_{1450} = -28.50$ of Onken et al. (2021) has been added for comparison in Figure 2, but it cannot be used during the fitting procedure, since it is not independent from the space density in QUBRICS. It shows however a good agreement with the best fit of $\gamma = -0.25$.

If we use all the data points from $z = 2.9$ to $z = 6.0$, then the resulting best-fit parameter is much steeper, $\gamma = -0.69$, indicating an accelerated evolution of the space density of bright QSOs at $z > 5$. If we limit the analysis to $z \geqslant 5.0$, then the redshift evolution of $\Phi(z)$ is even more pronounced, with $\gamma = -0.78$. Interestingly, limiting the redshift to $z \geqslant 4.5$, the evolution is even more dramatic, with a best fit of $\gamma = -0.91$. These latter values are compatible with the independent estimates carried out in the past by Ross et al. (2013; $\gamma = -0.809$) and by Yang et al. (2016; $\gamma = -0.81$).

We have collected on the top of Figure 2 the space densities Φ at a fainter absolute magnitude of $M_{1450} = -23.0$, in order to check whether the redshift evolution of the faint side of the AGN luminosity function is similar to the bright one. Of course, the statistics of faint AGNs at very high redshifts mainly rely on photometric redshifts derived from multi-wavelength data and often lack spectroscopic confirmation. In these cases the X-ray detection is a valuable criterion to include a Lyman break galaxy or a Lyα emitter in the high-redshift AGN population (e.g., Fiore et al. 2012; Giallongo et al. 2015; Boutsia et al. 2018; Giallongo et al. 2019; Grazian et al. 2020). We have included in Figure 2 the space densities derived from our CANDELS and COSMOS surveys. We have also included the recent results obtained by the SC4K survey (Santos et al. 2021) at $z = 3.1 \pm 0.4$, $z = 4.7 \pm 0.2$, and $z = 5.4 \pm 0.5$. The latter is based on 12 medium band and 4 narrowband filters used to select LAEs at various redshifts. The AGN fraction within the LAE sample has been selected by means of strong X-ray or radio detection, as detailed in Santos et al. (2021). It is worth noting the remarkable agreement of the space densities derived at about the same redshifts by our faint surveys, mainly based on broadband photometry, and the CS4K survey, based on narrowband photometry where the redshift accuracy is higher, thanks to the emission line detection. Finally, we have included the faint color-selected AGN sample by Kashikawa et al. (2015) at $z = 6.0$. Although limited by a simple and conservative color selection, it allows an extension of the analysis to the highest redshifts available for a faint AGN sample.

At $3 \leqslant z \leqslant 5.5$, the best-fit parameter of the redshift evolution at $M_{1450} = -23.0$ is $\gamma = -0.27$, comparable with the one at brighter luminosities. The dashed line in Figure 2 (top) indicates the resulting best fit to the $z \leqslant 5.5$ data at $M_{1450} = -23.0$. If we include the data by Kashikawa et al. (2015) at $z = 6.0$, the slope is slightly steeper, with $\gamma = -0.33$, but not comparable to the rapid evolution at $z > 5$ found for brighter QSOs, as discussed above.

We can draw two main considerations from Figure 2:

1. The space densities of bright QSOs and faint AGNs at $3 \leqslant z \leqslant 5$ show a similar evolution in redshift, indicating that the QSO luminosity function plausibly follows a pure density evolution, i.e., with a rigid shift in its normalization.
2. The density evolution at $3 \leqslant z \leqslant 5$ is milder than previous determinations, with a best-fit parameter of $\gamma = -0.25$.

The data at $z > 5.5$ in Figure 2 at bright luminosities seem to be compatible with an accelerated evolution of the space density of luminous QSOs with respect to $z < 5.5$. It is possible, however, that the different density evolution shown in

Figure 2 is due to an incompleteness of the surveys at $z \gtrsim 5$ or due to an underestimation of the incompleteness factors. Recent surveys (Schindler et al. 2019b; Boutsia et al. 2021), indeed, have shown that the first attempts to measure the space densities of bright QSOs at high z by the SDSS could possibly suffer from incompleteness by a large amount of ∼30−40% at $z \sim 4$, reaching a factor of 3 incompleteness at $z \sim 5$ (Wolf et al. 2020; Onken et al. 2021). If such an incompleteness is also affecting the data points at $z > 5$, and plausibly the incompleteness is stronger at $z \sim 6$ than at $z \sim 5$, then the observed drop could only be due to a spurious trend. Future investigations on the number densities of very bright QSOs at $z > 5$ will confirm or reject this hypothesis.

3.3. The Ionizing Background Produced by QSOs at z ∼ 5

The photoionization rate $\Gamma_{\rm HI}$ produced by bright QSOs and faint AGNs at $z \sim 5$ is derived here. We start from the recent determination of the $z \sim 4$ QSO luminosity function by (Boutsia et al. 2021, see their Table 4), rescaled to $z = 4.75$ with a pure density evolution, parameterized by the newly determined coefficient $\gamma = -0.25$, as discussed in the previous subsection.

Following the calculations carried out by Boutsia et al. (2021), we first derived the luminosity density at 1450 Å rest frame by integrating the QSO luminosity function, multiplied by the luminosity, from $M_{1450} = -30.0$ down to $M_{1450} = -18.0$. The exact value of the brighter integration limit does not significantly influence the total amount of the emissivity, since the bulk of UV photons are produced by AGNs with luminosity close to L^*, while the rare, very bright QSOs are contributing only to few percents of the total emissivity (Giallongo et al. 2019). We have assumed an escape fraction of Lyman continuum (LyC) photons of 70%, in agreement with recent results by Cristiani et al. (2016), Grazian et al. (2018), Romano et al. (2019), and a spectral slope of $\alpha_\nu = -0.61$ at $\lambda > 912$ Å rest frame and $\alpha_\nu = -1.7$ at $\lambda \leqslant 912$ Å rest frame, in agreement with Lusso et al. (2015). The mfp at $z = 4.75$ is 17.4 proper Mpc, following the relation by Worseck et al. (2014). We consider also the factor of 1.2 due to radiative recombination in the IGM (D'Aloisio et al. 2018). Using the same formalism adopted by Lusso et al. (2015), we obtain, from the AGN emissivity, a photoionization rate at $z = 4.75$ of $\Gamma_{\rm HI} = 0.46^{+0.17}_{-0.09} \times 10^{-12} s^{-1}$, shown as a blue square in Figure 3.

Comparing this value with the recent estimates of the ionizing UV background at these redshifts summarized in Table 3 and shown in Figure 3, it turns out that $z \sim 5$ AGNs are able to produce ∼50–90% of the LyC photons. This fraction can reach ∼100% if we consider the uncertainties on the QSO contribution to $\Gamma_{\rm HI}$ and the variance on the determination of the photoionization rate measured by the Lyman forest or by the proximity effects (e.g., Wyithe & Bolton 2011; Calverley et al. 2011; Davies et al. 2018). Thus, it emerges from these calculations that the contribution by $z \sim 5$ AGNs to the ionizing background is probably not negligible. In the next section we will discuss the implications of the LyC escape fraction and the faint-end slope of the QSO luminosity function on the estimate of the photoionization rate produced by high-z AGNs.

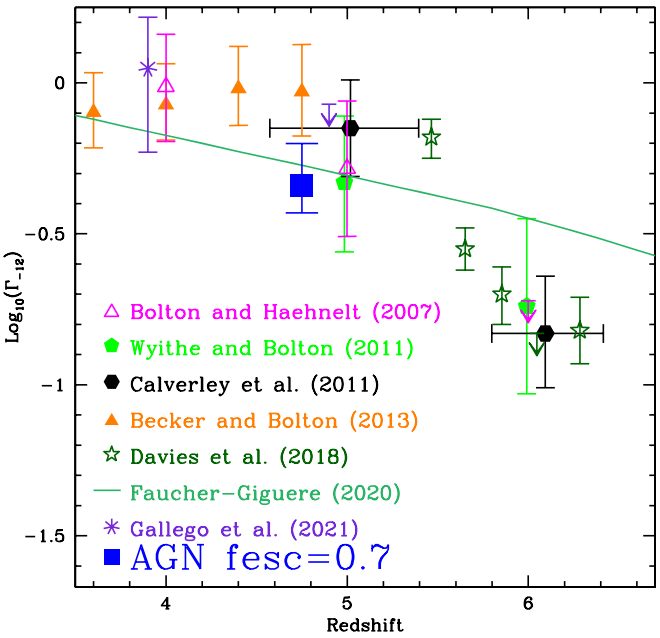

Figure 3. The photoionization rate $\Gamma_{\rm HI}$ (in units of $10^{-12} s^{-1}$) produced by the AGN population at $z \sim 5$ (blue square), assuming a Lyman Continuum escape fraction of 70% and a pure density evolution of the QSO luminosity function with $\gamma = -0.25$. A collection of the photoionization rates from different methods (e.g., Lyα forest fitting, proximity effect, QSO near zone size) has been carried out for comparison. The green continuous line is the prediction of the model by Faucher-Giguère (2020).

4. Discussion

4.1. The Reliability of the QUBRICS QSO Luminosity Function at z ∼ 5

The space density of luminous QSOs at $z > 4.5$ of the QUBRICS survey shown in Figure 1 is a factor of ∼3 higher than previous estimates. Since it is based on a wide area, covering approximately one third of the whole sky, it is implausible that cosmic variance plays a role in overestimating the bright QSO counts. A similar result has been obtained also by Onken et al. (2021) at $z > 4.4$ in a sky area partially overlapping with the QUBRICS survey. The reason for the huge discrepancies with respect to previous surveys is probably due to more efficient and complete selection criteria on the recent surveys, as shown by Schindler et al. (2019b) at $z > 3$ or by Boutsia et al. (2021) at $z \sim 4$.

There are indications, on the contrary, that the present determination of the space density could be even higher for a number of reasons:

1. The colors of $z \sim 5$ QSOs are similar to late-type stars. In order to gain efficiency in the selection of QSO candidates for spectroscopic confirmations, stringent color criteria have been adopted (e.g., McGreer et al. 2018; Matsuoka et al. 2018). A price to be paid in order to have high spectroscopic efficiency is the low completeness of the adopted selection criteria.
2. Several high-quality candidates based on colors or CCA criterion still need to be spectroscopically identified yet. Two bona-fide QSO candidates with $z_{CCA} > 4.5$, and three high-quality candidates with $z_{\rm XGB} > 4.5$ or selected with PRF have not been spectroscopically observed yet.
3. The space density shown in Figure 1 is based on the CCA selection criterion (Calderone et al. 2019; Boutsia et al. 2020), which has not been tuned to be particularly complete at $z > 4.5$, but has been designed to have high efficiency in a broader redshift range, i.e., at $z > 2.5$. The CCA selection indeed recovers only 5 of the 14 QSOs known and discovered in the QUBRICS footprint (see Table 1). The QUBRICS team is currently exploring

Table 3
The Photoionization Rate Γ_{HI} at $z \sim 5$

Reference	Method	redshift	Γ_{HI} in $10^{-12}s^{-1}$	$+\sigma_{\Gamma_{HI}}$	$-\sigma_{\Gamma_{HI}}$
THIS WORK ($\gamma = -0.25$)	AGN	4.75	0.46	+0.17	−0.09
Bolton & Haehnelt (2007)	Lyα forest	5.00	0.52	+0.35	−0.21
Wyithe & Bolton (2011)	QSO near-zone size	4.985	0.47	+0.31	−0.19
Calverley et al. (2011)	Proximity effect	5.02	0.71	+0.32	−0.22
Becker & Bolton (2013)	Lyα forest	4.75	0.94	+0.40	−0.27
Faucher-Giguère (2020)	Model	4.80	0.525	·	·
Gallego et al. (2021)	Fluorescent Lyα	4.9	<0.85	·	·

Note. The value of the ionizing background produced by AGNs has been estimated through the best-fit luminosity function of Boutsia et al. (2021) evolved at $z = 4.75$ with a pure density evolution with $\gamma = -0.25$.

different selection criteria, e.g., the probabilistic random forest (PRF; Guarneri et al. 2021) and the extreme gradient boosting (XGB; Calderone et al. in prep.), which could be tuned in order to have high completeness at $z > 4.5$.

Based on the above considerations, it is easy to conclude that the QSO luminosity function shown in Figure 1 is not the final measurement at $z > 4.5$ and at bright UV magnitudes ($M_{1450} \lesssim -28$). Recent attempts to find bright QSOs at $z > 4.5$ are under way (e.g., Wolf et al. 2020; Wenzl et al. 2021; Onken et al. 2021) and it is possible that additional $z \sim 5$ QSOs will be found in the near future in the QUBRICS footprint.

4.2. Uncertainties in the Estimate of the Photoionization Rate at z ∼ 5

The photoionization rate produced by bright QSOs and faint AGNs at $z = 4.75$ is relatively high, if the shape of the QSO luminosity function does not change from $z = 3.9$ to $z \sim 5$. A rigid shift of the QSO luminosity function with a pure density evolution seems to be confirmed by the data shown in Figure 2, where it is clear that the redshift evolution is similar both for bright QSOs and for faint AGNs. The new determinations of Φ by Onken et al. (2021) at $4.4 < z < 4.8$ and $4.8 < z < 5.5$ at the absolute magnitude $M_{1450} = -28.5$ are in agreement with the redshift evolution shown in Figure 2.

A pure density evolution of the AGN luminosity function at $z > 3$, however, is not in full agreement with the results of recent works which find a flatter slope for the faint end of the QSO luminosity function at high z (e.g., Matsuoka et al. 2018; Kulkarni et al. 2019; Kim & Im 2021). If the faint end of the $z \sim 5$ luminosity function is flatter than our extrapolations, the contribution of high-z AGNs to the ionizing background will be lower than our estimate in Table 3 and Figure 3.

In order to provide a quantitative estimate of the photoionization rate in the case of a flatter faint-end luminosity function, we consider the pure density evolution provided by Kim & Im (2021). According to their cases 1, 2, and 3, the AGN luminosity function at $z = 4.75$ is parametrized by a two-power law with slope $\alpha \sim -1$ and low space densities at $M_{1450} > -24$. Adopting their parameterizations for the luminosity function at $z = 4.75$, we obtain a photoionization rate of $\Gamma_{HI} = 0.058-0.063 \times 10^{-12}s^{-1}$. It corresponds to 6%−13% of the HI ionizing background measured at $z \sim 5$ (see Table 3). Thus, in case of a flat faint-end luminosity function at $M_{1450} > -24$, the contribution of QSOs and AGNs to the photoionization rate at $z \sim 5$ is not dominant.

It is worth noting, however, that the flat luminosity function by Kim & Im (2021) is in tension with the luminosity functions of Glikman et al. (2011) and Boutsia et al. (2018) at $z \sim 4$ and with the ones by Giallongo et al. (2019) and Grazian et al. (2020) at $z \sim 5.5$. Moreover, a flat luminosity function at $z \sim 5$ seems not fully compatible with the redshift evolution of the observed space densities, as summarized in Figure 2.

The determination of the photoionization rate by QSOs also depends on the Lyman continuum escape fraction of the AGN population. There are indications that this parameter is around 70% at $z \sim 4$, and it is almost constant both in luminosity (Grazian et al. 2018) and in redshift (Cristiani et al. 2016; Romano et al. 2019). Stacking thousands of SDSS QSOs at $3.5 \lesssim z \lesssim 5.5$, Prochaska et al. (2009) and Worseck et al. (2014) derived the mfp of HI ionizing radiation, assuming that the LyC escape fraction of these QSOs is close to 100%. The fact that their mfps are in agreement with the results of Inoue et al. (2014), based on the statistics of intergalactic absorbers, seems to indicate that $f_{esc}(LyC) \sim 100\%$, at least for very bright QSOs ($M_{1450} < -27$). For these reasons, we have assumed $f_{esc}(LyC) = 70\%$ for the entire luminosity regime where the QSO luminosity function has been integrated to compute the emissivity by active SMBHs.

High values of the escape fraction for high-z AGNs have been questioned by Micheva et al. (2017), who found $f_{esc}(LyC) \sim 30$–50% at $z \sim 3$ based on deep narrowband photometry at $\lambda \sim 3600$ Å. Recently, Iwata et al. (2022) have obtained an $f_{esc} = 0.36 \pm 0.10$ for $M_{1450} \leqslant -24$ AGNs at $z \sim 3.5$ and an $f_{esc} = 0.25 \pm 0.10$ for $M_{1450} > -24$. If we adopt the AGN luminosity function of Boutsia et al. (2021), evolved at $z = 4.75$ with a pure density evolution with $\gamma = -0.25$, and we consider the escape fraction by Iwata et al. (2022), we obtain a photoionization rate of $\Gamma_{HI} = 0.19 \times 10^{-12}s^{-1}$, which is 21%–41% of the HI ionizing background provided in Table 3. Thus, the contribution of high-z AGNs to the ionizing background still remains significant although not dominant, in the case of a low LyC escape fraction for AGNs.

It is possible, however, to reconcile the results of Micheva et al. (2017) and Iwata et al. (2022) with the one by Cristiani et al. (2016); Romano et al. (2019). The latter indeed measured the LyC escape fraction for >2000 QSOs at $z \geqslant 3.6$ at an absolute magnitude brighter than $M_{1450} \sim -27$, while the former adopted a sample of 94 AGNs at $3 < z < 4$ and $-26.5 \leqslant M_{1450} \leqslant -19.0$, with the bulk around $M_{1450} \sim -24$. Thus, the LyC escape fraction could show a mild

dependency on the absolute magnitudes of the AGNs, going from >70% at $M_{1450} \sim -28$ down to ~36% at $M_{1450} \lesssim -24$ and ~25% at $M_{1450} > -24$, as found by Iwata et al. (2022). It is worth noting, as discussed in Giallongo et al. (2019) and Boutsia et al. (2021), that the bulk of ionizing photons is produced by $L \geqslant L^*$ AGNs. If the escape fraction of faint AGNs is significantly lower than 70% at $M_{1450} \gtrsim -23$, we expect that the total ionizing radiation produced by the whole AGN population remains substantially high, close to 50%−100% of the photoionization rate. Based on these considerations, it turns out that the contribution of high-z AGNs to the ionizing background is probably not negligible at $z \sim 5$.

4.3. The QSO Luminosity Function at z ~ 6

The redshift evolution of the bright side of the QSO luminosity function from $z \sim 3$ to $z \sim 5$ is mild, with a best-fit parameter of $\gamma = -0.25$, as shown in Figure 2. The redshift evolution of the faint side from $z \sim 3$ to $z \sim 5$ is similar to the bright one, as can be seen from this figure. At $M_{1450} = -28.5$ there seems to be an accelerated evolution of the QSO space density from $z \sim 5$ to $z \sim 6$, with respect to the mild decrease observed at $z < 5.5$. This trend is evident with the drop of the bright end of the QSO luminosity function derived by Jiang et al. (2016). It is not clear, however, whether such a drop is due to a physical reason (faster accretion of the SMBH population) or, alternatively, if it is the effect of a strong incompleteness of past surveys. In the future it will be important to extend the present QSO surveys (Schindler et al. 2019a, 2019b; Wolf et al. 2020; Boutsia et al. 2021; Onken et al. 2021) at $z \sim 6$ in order to constrain the redshift evolution of the QSO luminosity function in a larger redshift interval.

It is interesting to note here that Calverley et al. (2011) inferred a mild decline in the emissivity of ionizing photons by roughly a factor of 2 between $z = 5$ and $z = 6$, by combining the measurements of the evolution of the mfp of ionizing photons with the evolution of the photoionization rate. If the ionizing UV background is entirely produced by QSOs and AGNs, then the result of Calverley et al. (2011) is fully consistent with a progression of a mild evolution of QSO luminosity function with $\gamma = -0.25$ even at $5 < z < 6$.

4.4. Strong Lensing Magnification?

An alternative explanation for the high space density of QSOs at ultrabright magnitudes could be interpreted also by the effect of strong lensing magnification of intrinsically fainter objects, as proposed by Pacucci & Loeb (2020). In the unlikely case that all the 14 QSOs of our sample are strongly magnified by large amplification factors, then the photoionization rate computed above could be no longer valid, and it is possible that the QSO population will be thus unable to provide the majority of the HI ionizing photons to maintain the IGM ionized at $z \sim 5$. Such conclusions depend on the exact amount and distribution of the magnification factors.

We have queried the Gaia EDR3 database (Gaia Collaboration et al. 2016, 2021) to check whether any of the 14 QSOs in Table 1 has a Gaia EDR3 counterpart within 3 arcsec, which could be an indication of strong lensing magnification. It turns out that none of the 14 QSOs at $z \sim 5$ has a nearby object. This could suggest that these QSOs are not strongly lensed by foreground objects, but a more careful analysis is needed before excluding strong lensing magnification as the reason for their exceptional luminosities. The strong lensing hypothesis could be verified in the future with high-resolution imaging of these ultrabright QSOs with JWST or with ELT.

5. Conclusions

The QUBRICS survey (Calderone et al. 2019; Boutsia et al. 2020, 2021; Guarneri et al. 2021) turns out to be particularly efficient and complete in the selection of ultrabright QSOs at high redshift ($z > 2.5$). Thanks to the extensive spectroscopic confirmations carried out progressing with this survey, and complementing our database with the results of other groups (Wolf et al. 2020; Onken et al. 2021), a sample of 14 ultrabright QSOs with $M_{1450} \leqslant -28.3$ at $4.5 < z_{\rm spec} < 5.0$ has been assembled in Table 1. Out of these 14 QSOs, 5 objects have a photometric redshift derived by the CCA technique of $z_{CCA} \geqslant 4.5$. With these 14 QSOs, the bright side of the luminosity function at $z \sim 5$ has been derived, as shown in Figure 1 and in Table 2.

From the QSO luminosity function at $z \sim 5$ in the QUBRICS footprint, and comparing them with similar results at $3 \lesssim z \lesssim 6$, we can derive a number of conclusions, which we summarize here:

1. At $z = 4.75$ the QSO space density in the absolute magnitude range $-29.3 \leqslant M_{1450} \leqslant -28.3$ is $\Phi = 3.115^{+1.077}_{-0.825} \times 10^{-10} cMpc^{-3}$.
2. This space density of QSOs at $z \sim 5$ and $M_{1450} = -28.6$ is a factor of 3 higher than previous determination in the past, as also recently derived by Schindler et al. (2019a, 2019b); Boutsia et al. (2021) at $z \sim 3-4$ and by Onken et al. (2021) at $z \geqslant 4.5$. This provides strong evidences that the previous results, mainly derived by the SDSS survey, may suffer by significant incompleteness, or their completeness corrections have been underestimated.
3. The bright-end slope of the $z \sim 5$ QSO luminosity function is relatively steep, with a best-fit value of $\beta = -4.64$, and an upper limit of $\beta \leqslant -3.4$ at 68% confidence level. There is no indication of a flattening of the bright-end slope of the QSO luminosity function going at high redshifts, as suggested by previous surveys.
4. The observed space density of ultrabright QSOs at $z \sim 5$ is not compatible with the recent best-fit parameterizations shown in Figure 1, which are underestimated by a factor of ~3 at $M_{1450} \sim -28.5$.
5. The redshift evolution of the space density of ultrabright QSOs ($M_{1450} \sim -28.5$) between $z = 4$ and $z = 5$ is milder than previous determinations. A fit to the space densities at $M_{1450} \sim -28.5$ in the redshift interval $3 \leqslant z \leqslant 5$ gives a mild logarithmic slope of $\gamma = -0.25$ (see Figure 2).
6. The evolution of the AGN space densities at much fainter luminosities of $M_{1450} \sim -23$ yields a similar best-fit parameter of $\gamma = -0.27$, indicating that at $z > 3$ the evolution of the QSO luminosity function is consistent with a pure density evolution law, i.e., a rigid shift toward lower values at higher redshift, with a uniform mild decline in the number density, independent of QSO luminosity.
7. Adopting a pure density evolution, we have evolved the QSO luminosity function of Boutsia et al. (2021) from $z = 3.9$ to $z = 4.75$, assuming $\gamma = -0.25$. The resulting luminosity function agrees with the QSO space density

from QUBRICS, as shown by the blue continuous curve in Figure 1.

8. The photoionization rate produced by bright QSOs and faint AGNs at $z\sim5$ in the absolute magnitude range $-30\leqslant M_{1450}\leqslant -18$ is $\Gamma_{\rm HI}=0.46^{+0.17}_{-0.09}\times10^{-12}s^{-1}$, assuming an escape fraction of 70% and a steep faint-end slope of the luminosity function ($\alpha=-1.85$), as derived by Glikman et al. (2011) and Boutsia et al. (2021) at $z\sim4$. This value of $\Gamma_{\rm HI}$ produced by AGNs is ∼50%−100% times the ionizing UV background measured at $z\sim5$ through different methods (e.g., Lyα forest, proximity effect, QSO near-zone size), as shown in Table 3.

This indicates that QSOs at $z\sim5$ do not have a marginal role in the production of ionizing photons detected at such high redshift, provided that their LyC escape fraction is high ($\geqslant$70%) and the faint end of the luminosity function is rather steep. Based on these results, a clear revision of the role of the AGN population in the cosmological reionization of hydrogen should be carried out. Paradoxically, the most enigmatic dark objects in the Universe, i.e., the SMBHs, could significantly contribute to the so-called First Light or Cosmic Dawn, ending the so-called Dark Ages.

Future spectroscopic wide-field instrumentation (e.g., WEAVE, 4MOST, Euclid) coupled with state-of-the-art imaging surveys (e.g., Rubin-LSST, Euclid, Roman Space Telescope) will extend the present analysis to lower luminosities and higher redshifts, providing a sound statistical sample of high-z QSOs. Armed with these data sets, it will be possible to study in detail the escape fraction of faint, high-z AGNs and the luminosity function of QSOs up to the Epoch of Reionization, and possibly even beyond.

We thank the referee for the useful comments that allowed us to improve the quality of the paper.

AG and FF acknowledge support from PRIN MIUR project black hole winds and the Baryon Life Cycle of Galaxies: the stone-guest at the galaxy evolution supper, contract 2017-PH3WAT.

Part of the results discussed in this work are based on observations made with the Italian Telescopio Nazionale Galileo (TNG) operated on the island of La Palma by the Fundacion Galileo Galilei of the INAF (Istituto Nazionale di Astrofisica) at the Spanish Observatorio del Roque de los Muchachos of the Instituto de Astrofisica de Canarias during periods AOT42 and AOT43.

This work is based on data products from observations made with ESO Telescopes at La Silla Paranal Observatory under ESO programmes ID 103.A-0746(A), 0103.A-0746(B), and 0104.A-0754(A).

This work has made use of data from the European Space Agency (ESA) mission Gaia (https://www.cosmos.esa.int/gaia), processed by the Gaia Data Processing and Analysis Consortium (DPAC; https://www.cosmos.esa.int/web/gaia/dpac/consortium). Funding for the DPAC has been provided by national institutions, in particular the institutions participating in the Gaia Multilateral Agreement.

This paper includes data gathered with the 6.5 meter Magellan Telescopes located at Las Campanas Observatory (LCO), Chile.

The national facility capability for SkyMapper has been funded through ARC LIEF grant LE130100104 from the Australian Research Council, awarded to the University of Sydney, the Australian National University, Swinburne University of Technology, the University of Queensland, the University of Western Australia, the University of Melbourne, Curtin University of Technology, Monash University and the Australian Astronomical Observatory. SkyMapper is owned and operated by The Australian National University's Research School of Astronomy and Astrophysics. The survey data were processed and provided by the SkyMapper Team at ANU. The SkyMapper node of the All-Sky Virtual Observatory (ASVO) is hosted at the National Computational Infrastructure (NCI). Development and support the SkyMapper node of the ASVO has been funded in part by Astronomy Australia Limited (AAL) and the Australian Government through the Commonwealth's Education Investment Fund (EIF) and National Collaborative Research Infrastructure Strategy (NCRIS), particularly the National eResearch Collaboration Tools and Resources (NeCTAR) and the Australian National Data Service Projects (ANDS).

This publication makes use of data products from the Wide-field Infrared Survey Explorer, which is a joint project of the University of California, Los Angeles, and the Jet Propulsion Laboratory/California Institute of Technology, funded by the National Aeronautics and Space Administration. This publication makes use of data products from the Two Micron AllSky Survey, which is a joint project of the University of Massachusetts and the Infrared Processing and Analysis Center/California Institute of Technology, funded by the National Aeronautics and Space Administration and the National Science Foundation.

Facilities: Skymapper, Wise, Gaia, Magellan:Baade (IMACS), Magellan:Clay (LDSS-3), TNG:Dolores, NTT:Efosc2.

ORCID iDs

Andrea Grazian https://orcid.org/0000-0002-5688-0663
Emanuele Giallongo https://orcid.org/0000-0003-0734-1273
Konstantina Boutsia https://orcid.org/0000-0003-4432-5037
Giorgio Calderone https://orcid.org/0000-0002-7738-5389
Stefano Cristiani https://orcid.org/0000-0002-2115-5234
Guido Cupani https://orcid.org/0000-0002-6830-9093
Fabio Fontanot https://orcid.org/0000-0003-4744-0188
Francesco Guarneri https://orcid.org/0000-0003-4740-9762
Yacob Ozdalkiran https://orcid.org/0000-0002-2881-1265

References

Abbott, T. M. C., Adamów, M., Aguena, M., et al. 2021, ApJS, 255, 20
Akiyama, M., He, W., Ikeda, H., et al. 2018, PASJ, 70, S34
Becker, G. D., & Bolton, J. S. 2013, MNRAS, 436, 1023
Becker, G. D., D'Aloisio, A., Christenson, H. M., et al. 2021, MNRAS, 508, 1853
Bolton, J. S., & Haehnelt, M. G. 2007, MNRAS, 382, 325
Bosman, S. E. I., Davies, F. B., Becker, G. D., et al. 2021, arXiv:2108.03699
Boutsia, K., Grazian, A., Calderone, G., et al. 2020, ApJS, 250, 26
Boutsia, K., Grazian, A., Fontanot, F., et al. 2021, ApJ, 912, 111
Boutsia, K., Grazian, A., Giallongo, E., Fiore, F., & Civano, F. 2018, ApJ, 869, 20
Bouwens, R. J., Illingworth, G. D., Franx, M., et al. 2009, ApJ, 705, 936
Bouwens, R. J., Oesch, P. A., Stefanon, M., et al. 2021, AJ, 162, 47
Cain, C., D'Aloisio, A., Gangolli, N., & Becker, G. D. 2021, ApJL, 917, L37
Calderone, G., Boutsia, K., Cristiani, S., et al. 2019, ApJ, 887, 268
Calverley, A. P., Becker, G. D., Haehnelt, M. G., & Bolton, J. S. 2011, MNRAS, 412, 2543

Cristiani, S., Serrano, L. M., Fontanot, F., Vanzella, E., & Monaco, P. 2016, MNRAS, 462, 2478
D'Aloisio, A., McQuinn, M., Davies, F. B., & Furlanetto, S. R. 2018, MNRAS, 473, 560
Davies, F. B., Bosman, S. E. I., Furlanetto, S. R., Becker, G. D., & D'Aloisio, A. 2021, ApJL, 918, L35
Davies, F. B., Hennawi, J. F., Bañados, E., et al. 2018, ApJ, 864, 142
Eilers, A.-C., Davies, F. B., Hennawi, J. F., et al. 2017, ApJ, 840, 24
Fan, X., Carilli, C. L., & Keating, B. 2006, ARA&A, 44, 415
Fan, X., Strauss, M. A., Schneider, D. P., et al. 2001, AJ, 121, 54
Faucher-Giguère, C.-A. 2020, MNRAS, 493, 1614
Finkelstein, S. L., D'Aloisio, A., Paardekooper, J.-P., et al. 2019, ApJ, 879, 36
Fiore, F., Puccetti, S., Grazian, A., et al. 2012, A&A, 537, A16
Gaia Collaboration, Brown, A. G. A., Vallenari, A., et al. 2021, A&A, 649, A1
Gaia Collaboration, Prusti, T., de Bruijne, J. H. J., et al. 2016, A&A, 595, A1
Gallego, S. G., Cantalupo, S., Sarpas, S., et al. 2021, MNRAS, 504, 16
George, E. M., Reichardt, C. L., Aird, K. A., et al. 2015, ApJ, 799, 177
Giallongo, E., Grazian, A., Fiore, F., et al. 2015, A&A, 578, A83
Giallongo, E., Grazian, A., Fiore, F., et al. 2019, ApJ, 884, 19
Glikman, E., Bogosavljević, M., Djorgovski, S. G., et al. 2010, ApJ, 710, 1498
Glikman, E., Djorgovski, S. G., Stern, D., et al. 2011, ApJL, 728, L26
Grazian, A., Giallongo, E., Boutsia, K., et al. 2018, A&A, 613, A44
Grazian, A., Giallongo, E., Fiore, F., et al. 2020, ApJ, 897, 94
Grazian, A., Giallongo, E., Gerbasi, R., et al. 2016, A&A, 585, A48
Grazian, A., Giallongo, E., Paris, D., et al. 2017, A&A, 602, A18
Guarneri, F., Calderone, G., Cristiani, S., et al. 2021, MNRAS, 506, 2471
Hoag, A., Bradač, M., Huang, K., et al. 2019, ApJ, 878, 12
Inoue, A. K., Shimizu, I., Iwata, I., & Tanaka, M. 2014, MNRAS, 442, 1805
Iwata, I., Sawicki, M., Inoue, A. K., et al. 2022, MNRAS, 509, 1820
Jiang, L., Fan, X., Annis, J., et al. 2008, AJ, 135, 1057
Jiang, L., McGreer, I. D., Fan, X., et al. 2016, ApJ, 833, 222
Kashikawa, N., Ishizaki, Y., Willott, C. J., et al. 2015, ApJ, 798, 28
Keating, L. C., Weinberger, L. H., Kulkarni, G., et al. 2020, MNRAS, 491, 1736
Kim, Y., & Im, M. 2021, ApJL, 910, L11
Kim, Y., Im, M., Jeon, Y., et al. 2020, ApJ, 904, 111
Kuhlen, M., & Faucher-Giguère, C.-A. 2012, MNRAS, 423, 862
Kulkarni, G., Worseck, G., & Hennawi, J. F. 2019, MNRAS, 488, 1035
Lusso, E., Worseck, G., Hennawi, J. F., et al. 2015, MNRAS, 449, 4204
Marshall, H. L., Tananbaum, H., Avni, Y., & Zamorani, G. 1983, ApJ, 269, 35
Masters, D., Capak, P., Salvato, M., et al. 2012, ApJ, 755, 169
Matsuoka, Y., Strauss, M. A., Kashikawa, N., et al. 2018, ApJ, 869, 150
McGreer, I. D., Fan, X., Jiang, L., & Cai, Z. 2018, AJ, 155, 131
Micheva, G., Iwata, I., & Inoue, A. K. 2017, MNRAS, 465, 302
Morales, A., Mason, C., Bruton, S., et al. 2021, ApJ, 919, 120
Naidu, R. P., Tacchella, S., Mason, C. A., et al. 2020, ApJ, 892, 109
Niida, M., Nagao, T., Ikeda, H., et al. 2020, ApJ, 904, 89
Oesch, P. A., Bouwens, R. J., Illingworth, G. D., Labbé, I., & Stefanon, M. 2018, ApJ, 855, 105
Onken, C. A., Wolf, C., Bian, F., et al. 2021, arXiv:2105.12215
Pacucci, F., & Loeb, A. 2020, ApJ, 889, 52
Pahl, A. J., Shapley, A., Steidel, C. C., Chen, Y., & Reddy, N. A. 2021, MNRAS, 505, 2447
Péroux, C., Storrie-Lombardi, L. J., McMahon, R. G., Irwin, M., & Hook, I. M. 2001, AJ, 121, 1799
Planck Collaboration, Aghanim, N., Akrami, Y., et al. 2020, A&A, 641, A6
Prochaska, J. X., Worseck, G., & O'Meara, J. M. 2009, ApJL, 705, L113
Reichardt, C. L., Patil, S., Ade, P. A. R., et al. 2021, ApJ, 908, 199
Riechers, D. A., Walter, F., Carilli, C. L., et al. 2006, ApJ, 650, 604
Robertson, B. E., Ellis, R. S., Furlanetto, S. R., & Dunlop, J. S. 2015, ApJL, 802, L19
Romano, M., Grazian, A., Giallongo, E., et al. 2019, A&A, 632, A45
Ross, N. P., McGreer, I. D., White, M., et al. 2013, ApJ, 773, 14
Santos, S., Sobral, D., Butterworth, J., et al. 2021, MNRAS, 505, 1117
Schindler, J.-T., Fan, X., Huang, Y.-H., et al. 2019b, ApJS, 243, 5
Schindler, J.-T., Fan, X., McGreer, I. D., et al. 2019a, ApJ, 871, 258
Storrie-Lombardi, L. J., McMahon, R. G., Irwin, M. J., & Hazard, C. 1996, ApJ, 468, 121
Véron-Cetty, M. P., & Véron, P. 2010, A&A, 518, A10
Wenzl, L., Schindler, J.-T., Fan, X., et al. 2021, AJ, 162, 72
Willott, C. J., Delorme, P., Reylé, C., et al. 2010, AJ, 139, 906
Wolf, C., Hon, W. J., Bian, F., et al. 2020, MNRAS, 491, 1970
Worseck, G., Prochaska, J. X., O'Meara, J. M., et al. 2014, MNRAS, 445, 1745
Wyithe, J. S. B., & Bolton, J. S. 2011, MNRAS, 412, 1926
Yang, J., Wang, F., Wu, X.-B., et al. 2016, ApJ, 829, 33
Zhu, Y., Becker, G. D., Bosman, S. E. I., et al. 2021, ApJ, 923, 223